ZnSe/N-doped Carbon Nanoreactor with multiple adsorption sites for Stable Lithium-Sulfur Batteries

Dawei Yang, Chaoqi Zhang*, Jordi Jacas Biendicho, Xu Han, Zhifu Liang, Ruifeng Du, Junshan Li, Jordi Arbiol, Jordi Llorca, Yingtang Zhou*, Joan Ramon Morante, Andreu Cabot*

D. W. Yang, C. Q. Zhang, Dr. J. J. Biendicho, Prof. J. R. Morante, Prof. A. Cabot
Catalonia Institute for Energy Research - IREC
Sant Adrià de Besòs, Barcelona, 08930, Spain
Email: czhang@irec.cat, acabot@irec.cat

D. W. Yang, C. Q. Zhang, R. F. Du, Dr. J. S. Li, Prof. J. R. Morante
Department of Electronic and Biomedical Engineering
Universitat de Barcelona, 08028 Barcelona, Spain

X. Han, Z. F. Liang, Prof. J. Arbiol
Catalan Institute of Nanoscience and Nanotechnology (ICN2)
CSIC and BIST, Campus UAB, Bellaterra, 08193 Barcelona, Spain

Prof. J. Llorca
Institute of Energy Technologies, Department of Chemical Engineering and Barcelona Research Center in Multiscale Science and Engineering
Universitat Politècnica de Catalunya, EEBE, 08019 Barcelona, Spain.

Prof. Y. T. Zhou
Key Laboratory of Health Risk Factors for Seafood and Environment of Zhejiang Province
Institute of Innovation & Application
Zhejiang Ocean University, Zhoushan, Zhejiang Province, 316022, China
Email: zhouyingtang@zjou.edu.cn

Prof. J. Arbiol, Prof. A. Cabot
ICREA
Pg. Lluís Companys 23, 08010 Barcelona, Spain

Abstract

The inhibition of this polysulfide shuttle effect and the promotion of the redox reaction kinetics remains as the key material challenges of lithium-sulfur batteries (LSBs) to be urgently solved. Here we report a new architecture for the cathode material based on nanoreactor of ZnSe/N-doped hollow carbon (ZnSe/NHC). This material combination and the hollow geometry provide three key benefits to the LSBs cathode: i) The combination of lithiophilic sites of NHC and sulfiphilic sites of ZnSe effectively trap LiPS as demonstrated by experimental results and density functional theory (DFT) calculations; ii) In part related to this promoted adsorption, the ZnSe/NHC material combination is able to facilitate the Li^+ diffusion, thus promoting the redox reaction kinetics; iii) The hollow nanoreactor design traps LiPS and accommodates volumetric expansion preventing the cathode material decomposition. As a result, LSBs cathodes based on this hybrid material, S@ZnSe/NHC, are characterized by high initial capacities, 1475 mAh g^{-1} at 0.1 C and 542 mAh g^{-1} at 3 C, and excellent rate capability. Besides, these cathodes deliver stable operation with only 0.022% capacity decay per cycle after 800 cycles at 3 C. Even at high sulfur loading of 3.2 mg cm^{-2}, a reversible capacity of 540.5 mAh g^{-1} is delivered after 600 cycles at 1 C. Overall, this work not only further demonstrates the large potential of transition-metal selenides as cathode materials in LSBs, but also demonstrates the nanoreactor design to be a highly suitable architecture to enhance cycle stability.

1. Introduction

Lithium-sulfur batteries (LSBs) have emerged as one of the most promising energy storage technologies owing to their potential low cost and high theoretical energy density (2600 Wh kg^{-1}) compared to lithium-ion batteries (420 Wh kg^{-1}). [1-3] While large progress has been achieved in recent years, a number of challenges remain to be overcome to commercially realize their potential. First, the poor conductivity of sulfur and lithium sulfide results in a sluggish electron transport, which requires adding a high electrical conductivity support to the cathode. Besides, the severe volumetric expansion during lithiation causes the pulverization of the sulfur cathode and the detachment of part of the active material from the conducting framework, what calls for a strategy to contain the expansion and/or the active material. [4-6] Additionally, the dissolution of intermediate lithium polysulfides (LiPS) into the electrolyte has associated a low coulombic efficiency (CE) and a rapid decline of capacity with cycling. Overcoming this limitation requires developing an efficient approach to immobilize the LiPS and enhance their redox kinetics. [7,8]

One effective strategy to improve the electrochemical performance of LSBs is to use carbon-based materials such as porous carbon, [9] graphene, [10,11] carbon spheres, [12] carbon nanotubes, [13,14] and nanofibers, [15] as high electrical conductivity sulfur host at the cathode. However, while carbon materials facilitate electron transport and transfer at the cathode, they are not able to suppress polysulfide shuttling owing to the weak chemical interaction between nonpolar carbons and polar LiPS. [16,17] Therefore, carbon-sulfur composites generally suffer from rapid capacity decays during cycling.

To promote interaction with LiPS, some polar inorganic materials have been recently considered as cathode materials, including transition metal oxides. [18,19] hydroxides, [20] carbides, [21] nitrides, [22] and sulfides. [23-25] These polar materials offer abundant LiPS adsorption sites and can even accelerate the catalytic conversion of LiPS to sulfur and solid Li-S phases, Li_2S_2/Li_2S, thus strongly reducing the loss of sulfur. [26,27] However, most metal oxides and sulfides have inherently poor electrical conductivities, which result in a low sulfur utilization efficiency and a sluggish redox reaction kinetics upon cycling.

Transition metal selenides (TMSe), such as $NiCo_2Se_4$ and Sb_2Se_3, are emerging as promising candidates to host sulfur at LSBs cathodes. [28,29] Compared with oxides and sulfides, selenides are characterized by higher electrical conductivities, similar polarities and in some cases enhanced catalytic activities. However, owing to their relatively high volumetric density,

TMSe need to be combined with high surface area carbon materials to achieve efficient utilization. In this direction, Zhang et al. recently demonstrated a graphene/$CoSe_2$ composited with superb electrocatalytic properties toward polysulfide redox reactions at triple-phase interfaces. [30] To step further beyond the state of the art, the carbon support need to be optimized and the most suitable TMSe selected.

In terms of geometry, hollow structures and particularly hollow cages are a particularly interesting form of carbon. Hollow carbon materials can physically confine polysulfides, preventing the shuttle effect and promoting their conversion reaction. In terms of composition, the use of N-doped carbon can not only improve electrical conductivity, but also promote LiPS adsorption though Li-N chemical binding. [31] On the other hand, Zn compounds and particularly ZnO and ZnS have recently gained high interest as cathode material in LSBs owing to their good adsorption capability, notable catalytic activity toward polysulfide conversion and low cost. [32,33]

In this work, we hypothesize the yet unexplored selenide, ZnSe, to be an optimum candidate as sulfur host in LSBs when combined with hollow N-doped hollow carbon. We detail here the first synthesis of ZnSe nanoparticles decorating N-doped hollow polyhedrons (ZnSe/NHC). These particles are then tested as nanoreactors toward stable LSBs cathodes. The obtained results are rationalized with the help of density functional theory (DFT) calculations.

2. Results and discussion
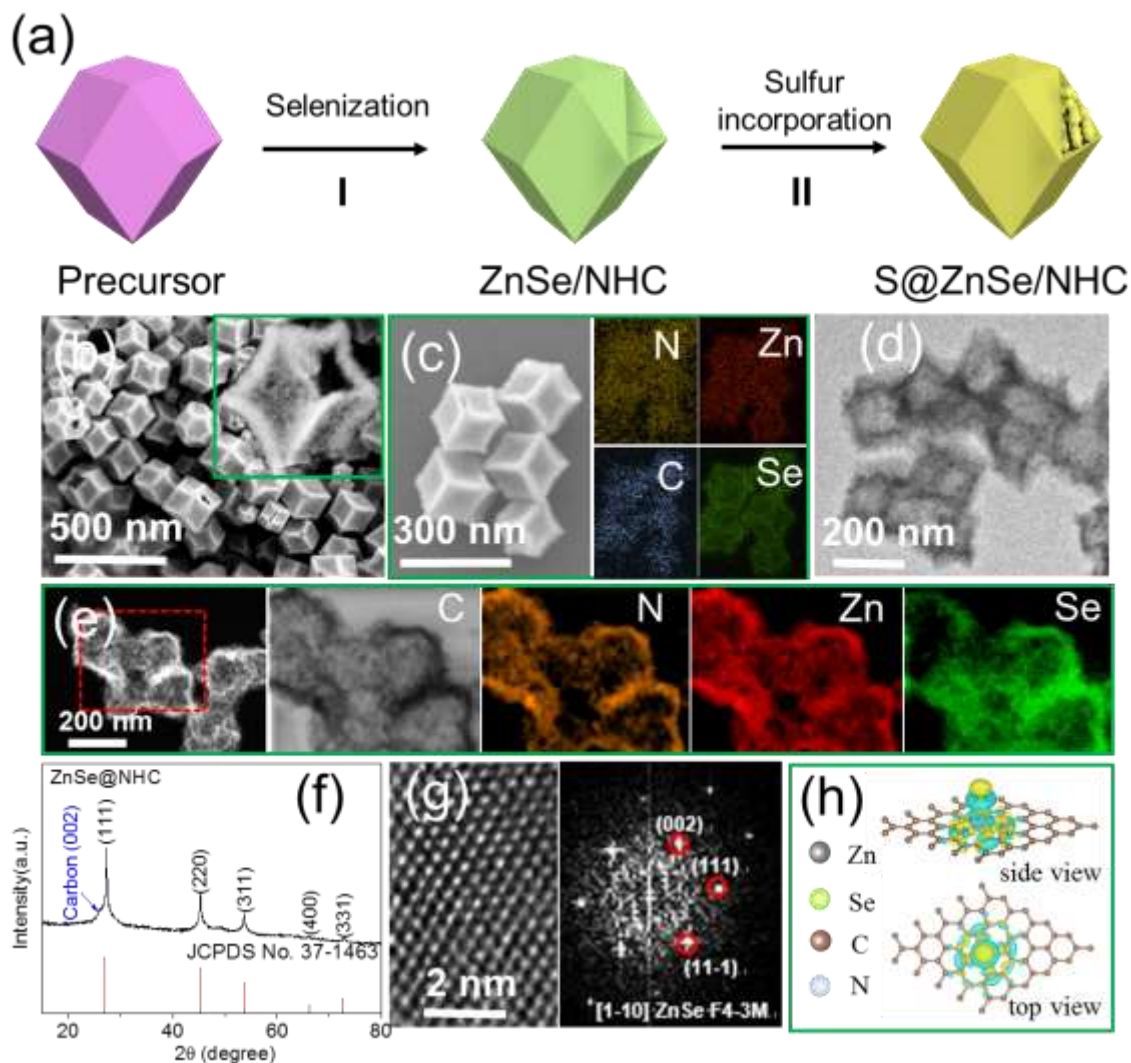
Figure 1. (a) Schematic illustration of the production of S@ZnSe/NHC composites. (b) FESEM image of ZnSe/NHC. Inset shows an enlarged hollow polyhedron. (c) SEM image and corresponding EDX elemental maps of N (yellow), Zn (red), C (blue), and Se (green). (d) TEM image of ZnSe/NHC. (e) STEM micrograph and corresponding EELS chemical composition maps. Individual C K-edge 284 eV (grey), N K-edge 401 eV (blue), Zn $L_{2,3}$-edge 1020 eV (red), and Se $L_{2,3}$-edge 1436 eV (green). (f) XRD pattern of ZnSe/NHC, including reference pattern for cubic ZnSe (JCPDS No. 37-1463). (g) HRTEM image of ZnSe/NHC and corresponding FFT spectrum. ZnSe lattice fringe distances were measured to be 0.317 nm, 0.321 nm, and 0.285 nm, at 67.48° and 123.37° which was interpreted as the ZnSe cubic phase visualized along its [1-10]

zone axis. (h) Calculated charge density difference of ZnSe/NHC from the model displayed in Figure S2. The yellow and blue regions represent increased and decreased electron density, respectively.

A schematic illustration of the process to produce S@ZnSe/NHC is shown in **Figure 1a**. First, a ZIF-8 precursor powder with polyhedron-shaped particles was synthesized via a modified precipitation method (Supporting Information, Figure S1). In a second step, the obtained precursor was annealed in a Se atmosphere to produce ZnSe/NHC (see experimental section for details). Finally, sulfur was incorporated within ZnSe/NHC by means of a melt-diffusion process. SEM characterization revealed the ZnSe/NHC particles display a polyhedral geometry with empty interiors as observed from some partially broken particles, EDS and TEM characterization (Figure 1b,c, d). We believe the hollow structure to be originated as a consequence of the different diffusion rates of selenium and zinc species through the growing ZnSe/NHC shells. This mechanism of formation of hollow particles is known as the nanoscale Kirkendall effect. [34,35] EDS and EELS elemental maps showed C, N, Zn and Se to be homogenously distributed throughout the ZnSe/NHC cages (Figure 1c,e). XRD and HRTEM analyses showed the cubic ZnSe (JCPDS No.37-1463) as the only crystalline phase within ZnSe/NHC composites (Figure 1f,g). [36,37] DFT analysis of the electronic distribution within ZnSe/NHC was analyzed by DFT showed electrons to be transferred from ZnSe to NHC and to accumulate around N atoms (Figure 1h), referring to model of the charge density difference of ZnSe/NHC (Figure S2). This charge redistribution at the interface region might enhance electron mobility in the composite.

XPS survey analysis showed the presence of Zn, Se, C, N and O in the surface of ZnSe/NHC (Figure S3a). The presence of oxygen was attributed to the exposure of the sample to air during handling and transportation. [28,38] XPS analysis also showed the material Fermi level to lay within a band of states, consistently with the metallic character of carbon (Figure S3f). The Zn 2p XPS spectrum (Figure S3b) exhibited one doublet at 1044.4 (Zn $2p_{1/2}$) and 1021.4 eV (Zn $2p_{3/2}$) assigned to Zn^{2+} within a ZnSe chemical environment. [36,39] The Se 3d spectrum (Figure S3c) also displayed just one doublet at 54.7 eV (Se $3d_{3/2}$) and 53.8 eV ($3d_{5/2}$) associated to Se^{2-} within ZnSe. [40,41] The high-resolution C 1s spectrum (Figure S3d) was fitted using four bands. The main band, at 284.8 eV, was associated to C-C and it was used as reference. The N 1s spectrum (Figure S3e) displayed three bands at 398.2, 399.6 and 400.7 eV, which were

associated with pyridinic, pyrrolic and graphitic nitrogen, respectively. [42,43] The detection of relatively large amounts of nitrogen confirmed the successful incorporation of nitrogen into the carbon framework. The presence of nitrogen within the carbon material was of interest for the potential of this element to increase the local atomic disorder, producing additional defects in carbon and exposing more active sites. Additionally, N-doping increases the electron concentrations, which could improve the electrical conductivity. [44,45]
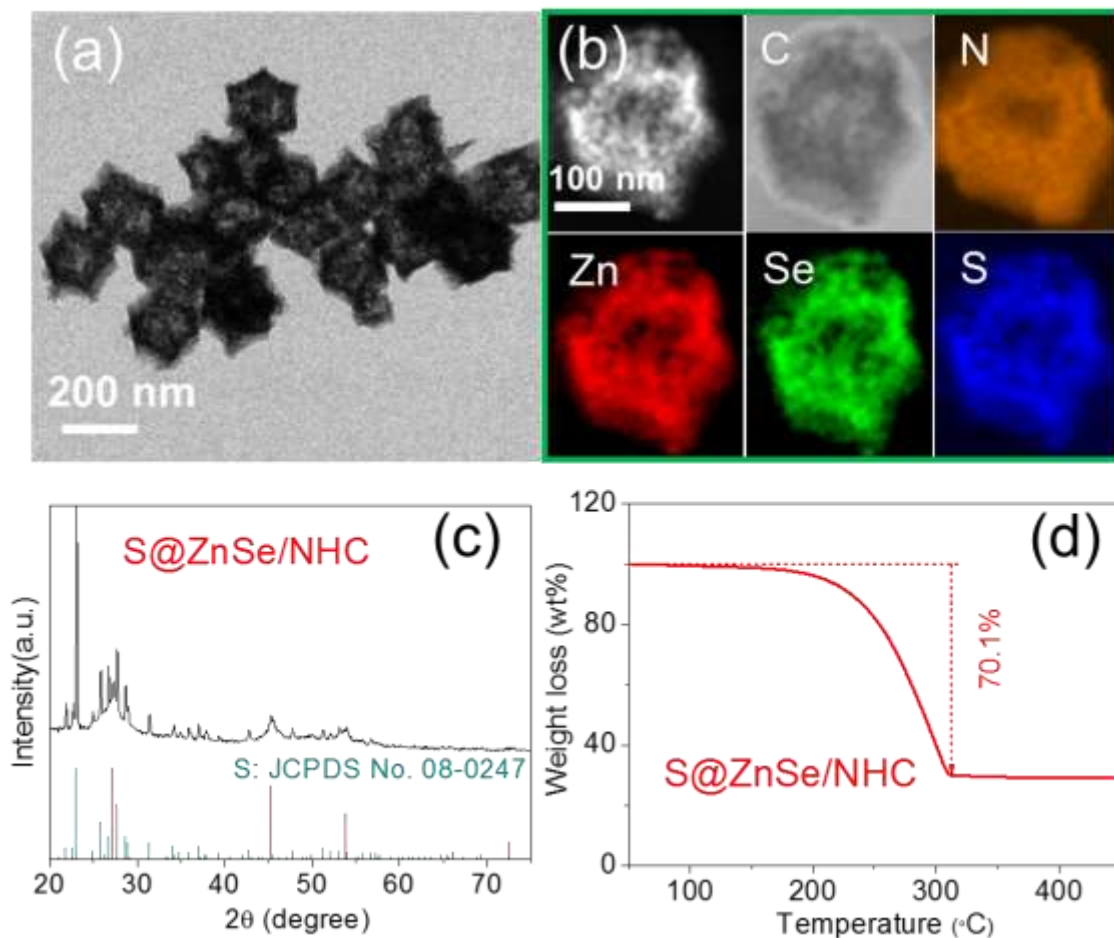
Figure 2. (a) Representative TEM image of a S@ZnSe/NHC composite. (b) STEM micrographs and corresponding EELS chemical composition maps. Individual C K-edge 284 eV (grey), N K-edge 401 eV (orange), Zn $L_{2,3}$-edge 1020 eV (red), Se $L_{2,3}$-edge 1436 eV (green), and S $L_{2,3}$-edge 165 eV (blue). (c) XRD pattern of S@ZnSe/NHC, including reference patterns for cubic ZnSe (JCPDS No. 37-1463) and cubic sulfur (JCPDS No. 08-0247). (d) TGA curve of S@ZnSe/NHC composite.

TGA analysis showed a mass decrease of ca. 70% when heating the sample up to 300 ºC, which was associated to the evaporation of sulfur and it was consistent with the nominal amount of sulfur introduced within ZnSe/NHC (Figure. 2d). S@ZnSe/NHC particles maintained the polyhedral geometry of ZnSe/NHC and ZIF-8 but displayed a partially filled structure (Figure S4a). To further verify the presence of sulfur within the hollow structures, nitrogen adsorption-desorption isotherms of the ZnSe/NHC cages before and after sulfur incorporation were measured (Figure S4b, c). The Brunauer–Emmett–Teller (BET) specific surface area was 275 m^2 g^{-1} for ZnSe/NHC, and decreased to 15.6 m^2 g^{-1} for S@ZnSe/NHC. In parallel, the overall pore volume decreased from 0.29 to 0.05 cm^3 g^{-1}, with the sulfur incorporation. These results further suggested the partial filling of the internal cavities of ZnSe/NHC. We believe the partially filled and partially empty voids to be advantageous in terms of buffering the volume change and trap polysulfides during the charge/discharge process. [46] Extensive TEM characterization discarded the presence of large sulfur aggregates outside the ZnSe/NHC cages (**Figure 2a**). EELS elemental maps further demonstrated the homogeneous distribution of sulfur within the cages (Figure 2b). XRD patterns of S@ZnSe/NHC displayed the presence of additional peaks that were indexed as cubic sulfur (Figure 2c). [20]
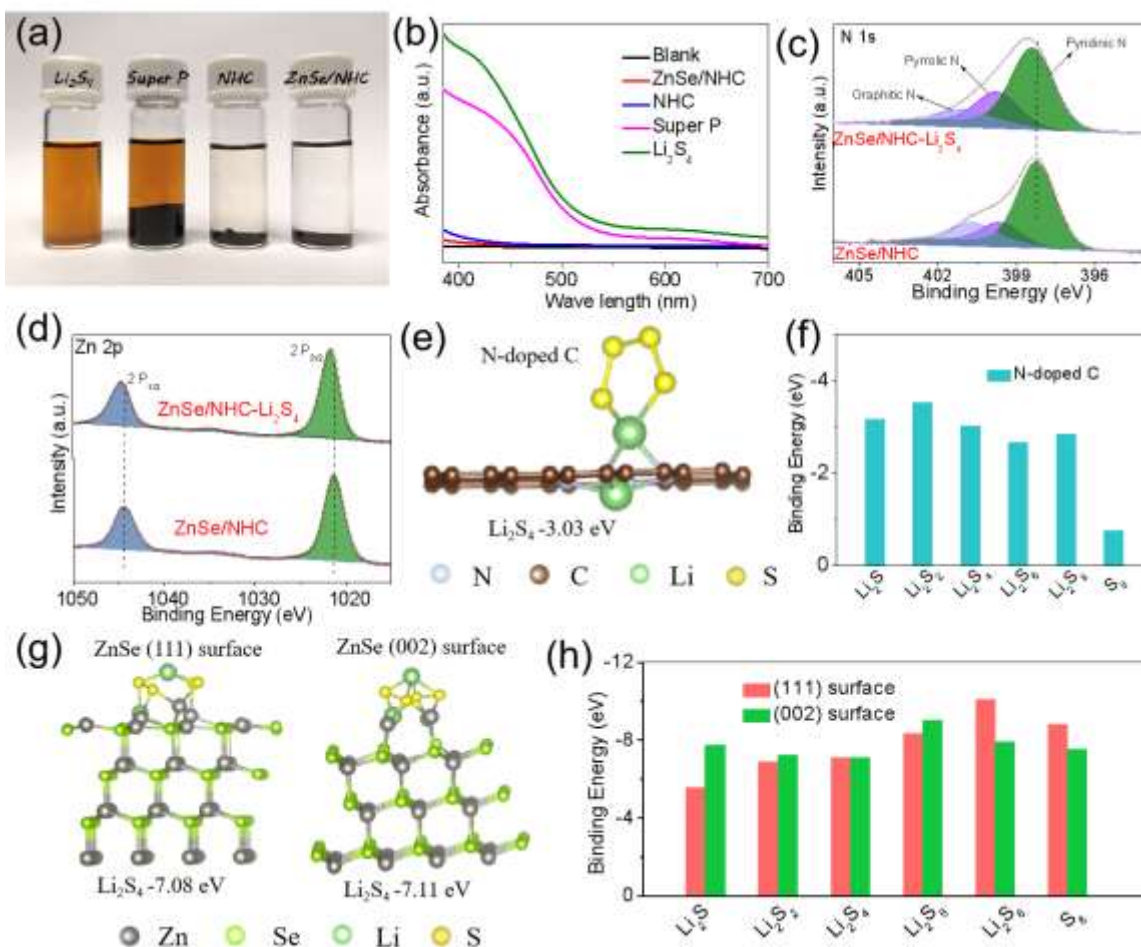
Figure 3. (a) Photograph of Li_2S_4 solutions containing (from left to right and as indicated in the figure): no adsorbant, Super P, NHC and ZnSe/NHC. (b) UV−Vis spectra of the polysulfide solution after overnight mixing with the different adsorbents. A blank spectrum and the spectrum of the Li_2S_4 solution not exposed to any adsorbant are also displayed. (c) N 1s and (d) Zn 2p XPS spectra of ZnSe/NHC before and after adsorption of Li_2S_4. (e) Adsorption configurations for Li_2S_4 on a N-doped C surface. (f) Calculated binding energy between LiPS (Li_2S, Li_2S_2, Li_2S_4, Li_2S_6, Li_2S_8 and S_8) and the N-doped C surface. (g) Optimized geometrical configurations of ZnSe with Li_2S_4 on both (111) and (002) surfaces. (h) Binding energies for LiPS (Li_2S, Li_2S_2, Li_2S_4, Li_2S_6, Li_2S_8 and S_8) on ZnSe surfaces calculated with DFT.

The Li_2S_4 adsorption ability of the host material was tested to evaluate its potential to confine LiPS. **Figure 3a** displays optical images of vials that initially contained a 10 mM

solution of Li_2S_4 and the same amount of ZnSe/NHC, Super P or NHC. After overnight mixing of the solutions, clear color differences were observed between the different vials. The Li_2S_4 solutions containing ZnSe/NHC and NHC displayed a much paler color than the solution containing Super P. This faded color was associated to a much more effective adsorption of Li_2S_4 on NHC and especially on ZnSe/NHC. UV-vis spectroscopy of the solution supernatants confirmed the notable differences of absorbance in the 400–500 nm region associated to Li_2S_4, [47,48] corroborating the different Li_2S_4 adsorption ability of the various host materials (Figure 3b).

Figure 3c displays the high-resolution N 1s XPS spectrum of ZnSe/NHC before and after the Li_2S_4 adsorption test (ZnSe/NHC-Li_2S_4). A clear shift of the N 1s bands was observed with the Li_2S_4 adsorption. We associate this shift with the binding of Li_2S_4 and N heteroatoms. This binding takes place through a dipole-dipole electrostatic interaction between Li atoms having a Lewis acid character within LiPS and N heteroatoms with extra pair of electrons in carbon materials and a Lewis base character. [44,49] This Li-N affinity provides NHC with a lithiophilic character that explains the high Li_2S_4 adsorption ability of NHC. Figure 3d displays the high-resolution Zn 2p XPS spectrum of ZnSe/NHC before and after the Li_2S_4 adsorption test. A slight shift of the Zn 2p bands to higher binding energies was also observed after Li_2S_4 adsorption. This shift was consistent with Zn being in a slightly more electronegative chemical environmental than within ZnSe, which we associate with a chemical interaction between Zn and sulfur. This Zn-S interaction, which adds up to the N-Li interaction, explains the higher Li_2S_4 adsorption ability of ZnSe/NHC when compared with NHC.

DFT calculations were conducted to understand the chemical anchoring process at the atomic level. The geometries of the adsorption configurations for LiPS at six different lithiation stages on a N-doped C surface are displayed in Figure S5. The binding energy (E_b) between LiPS species and ZnSe/NHC was calculated to evaluate the LiPS adsorption capability. Figure 3e displays a configuration of a Li_2S_4 molecule immobilized by Li-N bonds on N-doped C surface with a high E_b, -3.03 eV, suggesting a high lithiophilicity of NHC associated to the presence of N. Several adsorption configurations with significantly higher E_b than graphitic carbon demonstrated the affinity of N-doped C toward various LiPS species (Figure 3f). [50,51]

Several geometrically configurations of LiPS adsorbed at (111) and (002) facets of ZnSe are illustrated in Figure S6. Figure 3g shows the calculated E_b for Li_2S_4 anchored on ZnSe (111) and

(002) surfaces to be -7.08 eV and -7.11 eV, respectively. The E_b of additional LiPS adsorbed on the (111) and (002) surfaces of ZnSe are presented in Figure 3h. These DFT results demonstrated a strong interaction between S within LiPS and Zn within ZnSe, which corroborates the sulfiphilic character of ZnSe within ZnSe/NHC. Overall, both experimental results and DFT calculations proved ZnSe/NHC to have a high affinity toward LiPS, associated to the presence of a dual adsorption effect related to the presence of sulfiphilic sites on ZnSe and of lithiophilic sites on NHC.
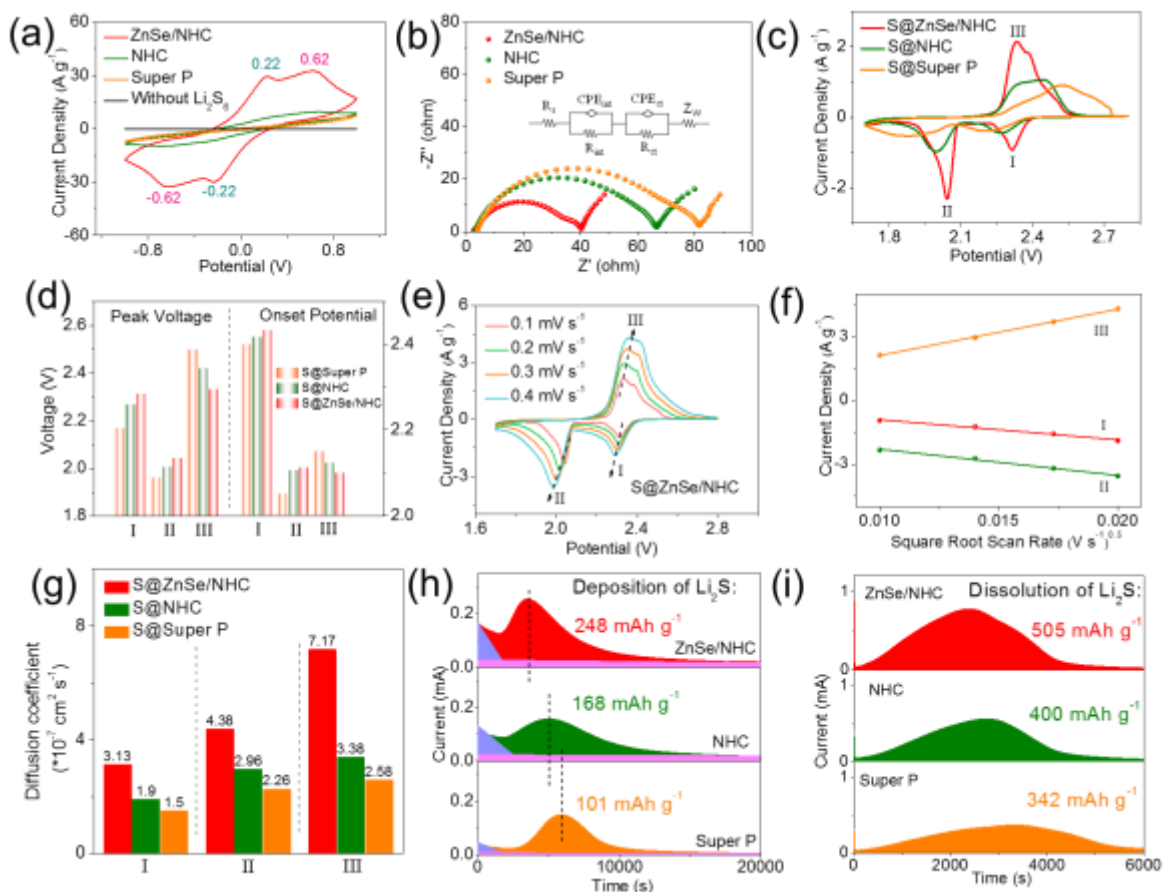
Figure 4. (a) CV curves at a scan rate of 20 mV s^{-1} of symmetrical cells using an electrolyte containing 0.5 mol L^{-1} Li$_2$S$_6$. (b) EIS curves of the same cells. Inset shows the fitted equivalent circuit. (c) CV curves of different electrodes at a scan rate of 0.1 mV s^{-1} within 1.7-2.8 V versus Li/Li$^+$. (d) Values of peak voltages and onset potentials of Li–S cells obtained from the CV curves. (e) CV curves of a S@ZnSe/NHC cathode at different scan rates. (f) CV redox peak current versus the square root of the scan rate. (g) Li$^+$ diffusion coefficient calculated from the

different CV redox peaks according to the Randles–Sevcik equation. (h) Potentiostatic discharge profiles with a Li_2S_8 solution at 2.05 V. (i) Potentiostatic charge profile at 2.40 V to evaluate dissolution kinetics of Li_2S.

In order to study the electrocatalytic activity of the materials, CV curves were measured from symmetric cells made using 0.5 mol L^{-1} Li_2S_6 and 1 mol L^{-1} LiTFSI dissolved in DOL/DME (v/v = 1/1) as electrolyte and identical ZnSe/NHC (NHC and Super P) electrodes as working and counter electrodes. To be able to eliminate the capacitive contribution, the CV of ZnSe/NHC in a Li_2S_6-free electrolyte was also measured as a reference (Figure S7a). As shown in **Figure 4a**, ZnSe/NHC cells displayed two pairs of reversible redox peaks at a scan rate of 20 mV s^{-1}. During discharge process, the reduction peaks at -0.22 V and -0.62 V were related with the reduction of S to Li_2S_6 and of Li_2S_6 to Li_2S, respectively. In the subsequent charge process, the oxidation peaks at 0.22 and 0.62 V corresponded to the oxidation of Li_2S to Li_2S_6 and of Li_2S_6 to S, respectively. [11,26] CV curves of ZnSe/NHC symmetric cells overlapped each other as shown for 10 cycles in Figure S7b, indicating an excellent reversibility. On the other hand, symmetric cells made of NHC and Super P-based electrodes exhibited much lower current densities and undefined redox peaks, demonstrating the essential role played by ZnSe in the electrochemical process (Figure 4a).

Results from EIS analysis of different symmetric cells after CV tests are displayed in Figure 4b. The equivalent circuit shown in the inset was used to fit Nyquist plots. The intersection of the curve with abscissa is assigned to the interphase-contact resistance of the electrolyte and the cells (R_s). The first semicircle in the high frequency is related to the charge transfer resistance (R_{ct}). The second semicircle in the middle frequency region is ascribed to the interface between the insulating layer of Li_2S and the electrode (R_{int}). Finally, the sloping lines in the low frequency region correspond to Warburg impedance (Z_w), which is related to the diffusion of lithium ions into the electrode. According to the fitting results (Figure S8), ZnSe/NHC cells delivered a lower R_{ct} (40.1 Ω) compared to NHC (67.8 Ω) and Super P (81.5 Ω), indicating enhanced charge and ion transfer, possibly due to their high conductivity. Besides, the R_{int} from the ZnSe/NHC cell (20.26 Ω) was much smaller the measured from NHC (45.82 Ω) and Super P (65.82 Ω). We associate this smaller R_{int} attributes to the uniform deposition of Li_2S on the surface of the electrodes.

Tafel plot analysis further demonstrated ZnSe/NHC electrodes to be characterized by a lower polarization potential and higher exchange current densities than the other electrodes, pointing toward an enhanced redox reaction kinetics in ZnSe/NHC (Figure S9).

Overall, the analysis of symmetric cells demonstrated that ZnSe/NHC was characterized by significantly enhanced polysulfide redox kinetics enabled by a much faster charge transfer kinetics at the ZnSe/NHC/polysulfide interface. [52-54]

CV curves of Li–S coin cells based on S@ZnSe/NHC cathodes are shown in Figure 4c. Data for the other electrodes with the same content of sulfur, S@NHC and S@Super P, can be found in Figure S10 and S11. CV curves measured from S@ZnSe/NHC cells almost overlaped during the first three cycles, implying a good reversibility of the sulfur redox reactions (Figure S12). S@ZnSe/NHC cathodes showed two representative cathodic peaks and one anodic peak. The two cathodic peaks (peak I and peak II) were associated with the reduction of S_8 molecules to long-chain polysulfides (peak I) and to the further reduction to short-chain sulfides (peak II). The broad anodic peak (Peak III) was ascribed to the multistep oxidation of short-chain sulfides eventually to S_8. [23,52] The S@ZnSe/NHC cathode displayed a more positive potential of the cathodic peaks (peak I at 2.301 and peak II at 2.035 V) and a more negative anodic peak (peak III at 2.355 V) than S@NHC and S@Super P (Figure 4d).

We further determined the onset potential as the potential required to reach a current density of 10 µA cm^{-2} beyond the baseline current as conventionally done in electrocatalysis (Figure S13 and 5d). [55,56] We observed the cells based on S@ZnSe/NHC cathodes to display higher onset potentials of reduction peaks and lower onset potentials of oxidation peaks than cells based on other materials, which is consistent with the promotion of the polysulfide redox kinetics by the presence of ZnSe/NHC.

CV tests at different scan rates from 0.1 to 0.4 mV s^{-1} were conducted to investigate the electrode reaction kinetics and the lithium ion diffusion properties of S@ZnSe/NHC, S@NHC and S@Super P cathodes. As shown in Figure 4e, with the increase of the scan rates, the peak current density of the S@ZnSe/NHC cathode increased, but its shape was maintained, denoting a good electrochemical stability. Besides, we observed a linear relationship between the cathodic and anodic peak currents and the square root of the scanning rate, as it corresponds to a diffusion-limited process (Figure 4f). From the fitting of this linear dependence, the diffusion

constant of the rate limiting species, i.e. lithium ions (D_{Li+}), was calculated according to the Randles–Sevcik equation: [28,57]

$$I_p = (2.69 * 10^5) n^{1.5} A D_{Li+}{}^{0.5} C_{Li+} v^{0.5}$$ **Equation 1**

Where I_p is the peak current density, n is the number of charge transferred, A is the geometric area of the electrode, C_{Li+} is the concentration of lithium ions in the cathode, and v is the scan rate. According to the Randles–Sevcik equation, the values of D_{Li+} calculated for S@ZnSe/NHC at peaks I, II, and III were 3.1×10^{-7}, 4.4×10^{-7}, and 7.2×10^{-7} cm^2 s^{-1}, respectively. Among the three materials tested, S@ZnSe/NHC electrodes exhibited the sharpest slopes, thus the fastest lithium ion diffusion in both reduction and oxidation processes (Figure S14). The enhanced lithium ion diffusivity may be related to two aspects: i) a higher catalytic activity that lowers the energy barriers for electron transfer; and ii) a strong polysulfide adsorption that reduces the electrolyte viscosity, increasing mobility of electrolyte species and avoiding the deposition of an insulating layer.

To further explore catalytic properties of the cathode materials, the Li$_2$S nucleation and dissolution was studied through potentiostatic measurements. As observed in Figure 4h, the presence of ZnSe clearly resulted in shorter nucleation and growth times and a higher discharging peak current during the potentiostatic measurement at 2.05 V. Based on the Faraday's law, the capacity of ZnSe/NHC electrodes was calculated at 248.2 mAh g^{-1}, well above that of NHC (168.5 mAh g^{-1}) and Super P electrodes (101.8 mAh g^{-1}). These results suggest that ZnSe significantly improved the kinetics of Li$_2$S precipitation. [30] To study the kinetics of the Li$_2$S dissolution step, the potentiostatic cell charge at 2.40 V was analyzed (Figure 4i). ZnSe/NHC cathodes resulted in significantly higher current densities compared to NHC and Super P, indicating its lower oxidation overpotential for Li$_2$S dissolution.[58.59] Furthermore, the capacity of Li$_2$S dissolution of ZnSe/NHC (505 mAh g^{-1}) was higher than NHC (400 mAh g^{-1}) and Super P (342 mAh g^{-1}).

After 20000 s potentiostatic discharge the coin cells were disassembled to further investigate the ability of ZnSe/NHC in regulating the nucleation of Li$_2$S. Interestingly, a layer of small Li$_2$S nanoparticles were uniformly distributed on the surface of ZnSe/NHC (Figure S15a). In contrast, Li$_2$S nanoparticles aggregated on the surface of Super P, forming a bulky structure (Figure S15b). The differences in the morphology were mainly related to the large density of lithiophilic and sulfiphilic nucleation sites on the surface of ZnSe/NHC, which captured

polysulfides and reduce the energy barrier of Li_2S nucleation. We believe this process significantly limited the shuttle effect. [30]

From the above results, it can be concluded that NHC and ZnSe with lithiophilic and sulfiphilic sites, respectively, are able to capture LiPS efficiently during redox reactions. The presence of ZnSe nanoparticles greatly boosts the reaction kinetics of LiPS.
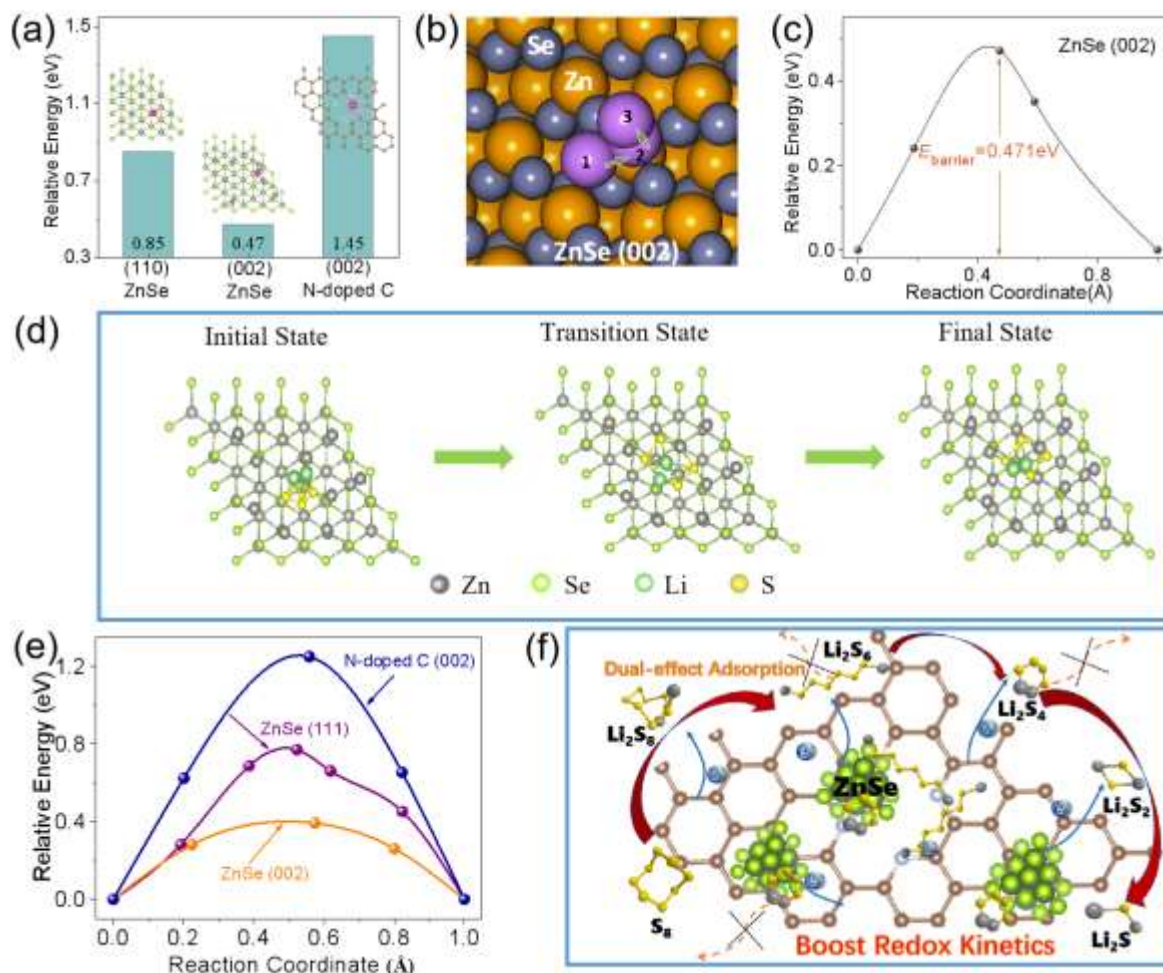
Figure 5. (a) Energy barrier of Li ion diffusion on (111) and (002) facets of ZnSe and (002) facet of N-doped C. (b) Geometrical configurations corresponded to the minimum energy path of Li ion diffusion on (002) facet of ZnSe. 1, 2 and 3 represent initial state, transition state and final state, respectively. (c) Energy profile for Li ion diffusion on (002) facet at different adsorption sites. (d) Illustration of stages of Li_2S_4 diffusing on a (002) facet of ZnSe. (e) Energy profiles of Li_2S_4 migration on (111) and (002) facets of ZnSe and (002) facet of N-doped C along different

adsorption sites. (f) Schematic illustration of the LiPS catalytic conversion on ZnSe during discharge process.

We further verified the boosted redox kinetics of LiPS catalytic conversion by DFT calculations. **Figure 5a**, S16 and S17 show the minimum energy barrier ($E_{barrier}$) of Li ion diffusion on three facets, suggesting Li ion diffused fastest on the (002) facet of ZnSe than on the other two facets. The schematic diagram of Li ion diffusion on (002) facet is displayed in Figure 5b. Figure 5c and S18 exhibit the $E_{barrier}$ of Li ion diffusion for different adsorption sites of the three facets. It was concluded that ZnSe diffuses fastest on the (002) facet, suggesting that the presence of ZnSe accelerates the diffusion of Li ion. Figure 5d, S19 and S20 show the initial state, transition state and final state of Li_2S_4 migration on the three facets. The $E_{barrier}$ of Li_2S_4 migration along different adsorption sites shown in Figure 5e and Figure S21 (Supporting Information). The $E_{barrier}$ for Li_2S_4 migration was calculated to be 0.392, 0.771 and 1.25 eV on (002), (111) and N-doped C surfaces, respectively. These results confirmed that ZnSe facilitated the migration of Li_2S_4. During the reaction process, LiPS species were anchored through the lithiophilic sites of NHC and sulfiphilic sites of ZnSe. This dual adsorption not only effectively suppressed the shuttle effect, but also accelerated the diffusion of Li^+/LiPS, thereby enhancing the LiPS conversion reaction kinetics (Figure 5f).
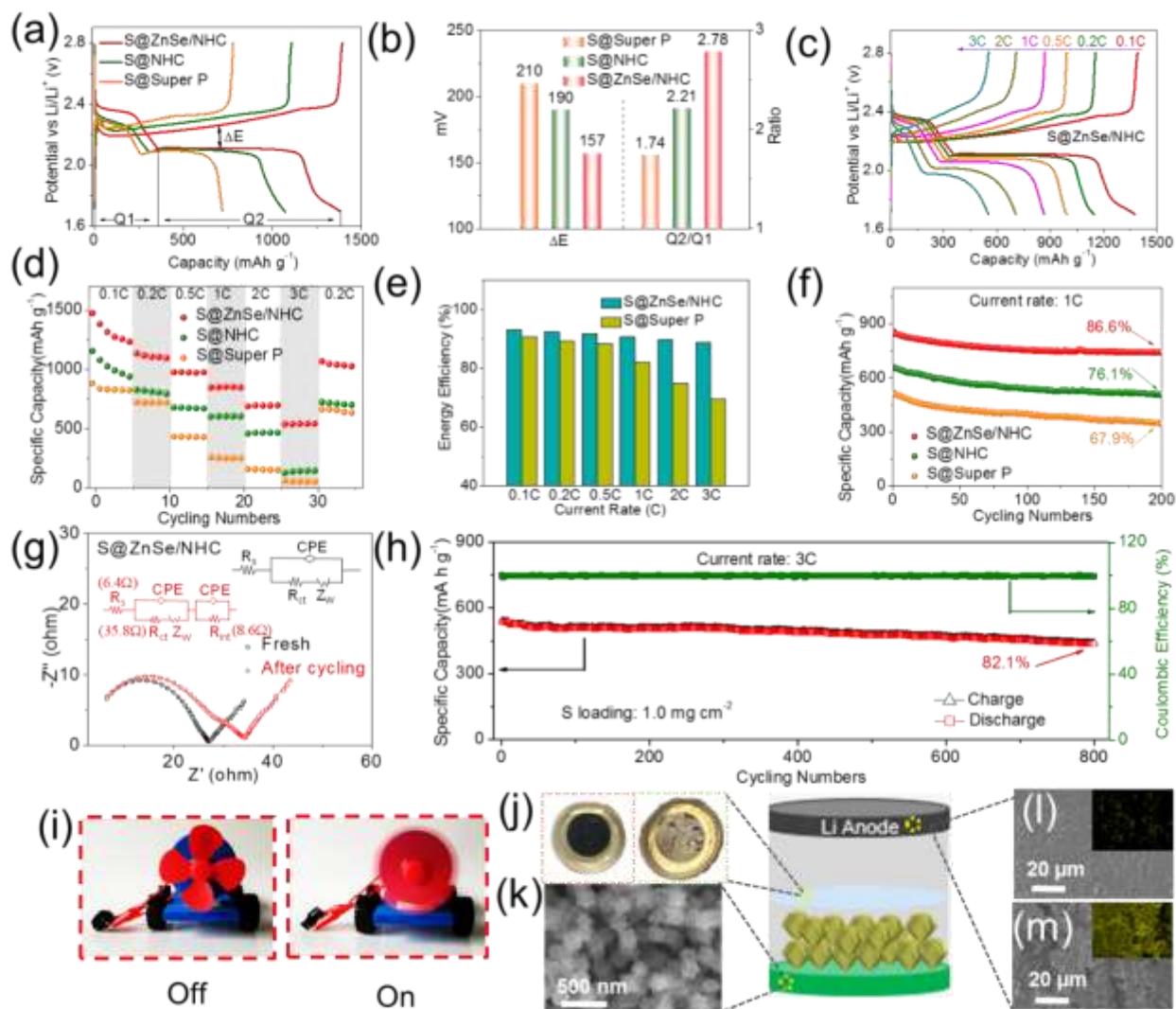
Figure 6. (a) Galvanostatic charge−discharge profiles of different electrodes at a current density of 0.1 C. (b) ΔE and Q2/Q1 calculated from the charge−discharge curves. (c) Galvanostatic charge−discharge profiles of S@ZnSe/NHC at different current densities range from 0.1 C to 3 C. (d) Rate capabilities of different electrodes at various current densities. (e) Energy efficiency of S@ZnSe/NHC compared with S@Super P. (f) Cycling life of various cathodes after 200 cycles at 1 C. (g) EIS spectrum of S@ZnSe/NHC cathode before and after 200 cycles at 1 C. (h) Cycling performances and corresponding CEs of S@ZnSe/NHC cathode at a high current rate of 3 C. (i) Digital photographs of wind car powered by one S@ZnSe/NHC Li−S coin cell. (j) Separators of coin cells with S@ZnSe/NHC as cathode (left) and S@Super P as cathode (right) after cycling at 1 C for 200 cycles. (k) SEM image of S@ZnSe/NHC cathode and (l, m) surface

of lithium foil from S@ZnSe/NHC and S@Super P coin cells. Inset images in (l, m) are EDX mapping images showing sulfur signal after cycling.

Electrochemical performance was further analyzed through galvanostatic charge–discharge tests. **Figure 6a** shows the charge–discharge curves of S@ZnSe/NHC, S@/NHC and S@Super P at a current density of 0.1 C. Charge–discharge curves displayed two discharge plateaus and one charge plateau. The voltage difference between the oxidation and the second reduction plateaus is the polarization potential, referred as ΔE. S@ZnSe/NHC showed lower polarization potential ($\Delta E = 157$ mV) than S@NHC ($\Delta E = 190$ mV) and S@Super P electrodes ($\Delta E = 210$ mV) as displayed in Figure 6b. [20,49] The first discharge plateau around 2.3 V is related to the reduction of sulfur to soluble LiPS ($S_8 \rightarrow S_6^{2-} \rightarrow S_4^{2-}$). The second discharge plateau, at about 2.1 V, corresponds to the conversion of soluble LiPS to lithium sulfide ($S_4^{2-} \rightarrow Li_2S_2 \rightarrow Li_2S$). [22,28] Defining Q1 and Q2 as the capacity of the first and second discharge plateaus, respectively, the ratio Q2/Q1provides an idea of the material catalytic activity. [28] The higher Q2/Q1, the better the catalytic ability, because Q1 measures the amount of soluble polysulfides created and potentially diffusing to the Li metal anode, while Q2 measures how efficiently polysulfides are reduced to Li_2S. [60,61] As shown in Figure 6b of the Q2/Q1 ratio for S@ZnSe/NHC was 2.68, well above the values obtained from S@NHC and S@Super P, 2.05 and 1.64,respectively. The high Q2/Q1 ratio further confirmed the superior catalytic activity towards polysulfides redox reaction of ZnSe/NHC. [60] The enhanced electrochemical kinetics of S@ZnSe/NHC compared with other electrodes was also in accordance with the lower measured overpotentials for phase conversion between the soluble LiPS and insoluble Li_2S_2/Li_2S during the discharge (Figure S22a) and charge (Figure S22b) processes.

The galvanostatic charge–discharge voltage profiles of S@ZnSe/NHC at various current densities range from 0.1 to 3 C are presented in Figure 6c, two discharge plateaus and one charge plateau were clearly maintained at the various current rates tested, which is in contrast to results obtained from S@NHC and S@Super P (Figure S23). A high initial specific capacity of 1475 mAh g^{-1} was delivered by the S@ZnSe/NHC electrode. Additionally, a superior rate performance of this electrode compared was inferred from the average discharge capacities of 1340, 1116, 977, 852, 696 and 542 mAh g^{-1} at current rates from 0.1 C to 3 C, respectively, which are well above than those obtained from S@NHC and S@Super P (Figure 6d). Even when the current density was returned to 0.2 C, the specific capacity of the S@ZnSe/NHC electrode

was recovered to 1068 mAh g^{-1}, suggesting a high stability even after the high rate charge−discharge process.

As shown in Figure 6e, cells based on S@ZnSe/NHC were also characterized by higher energy efficiencies, $E = \int UIdt$, compared to S@Super P. Energy efficiency is a key parameter in energy storage devices, [28] as it determines energy losses during charging/discharging process, especially at high current rates. The significant enhancement in energy efficiency obtained from ZnSe/NHC cells stemmed from the lower polarization potential, associated with the exceptional catalytic properties of the cathode material.

The cycling performance of different cathodes was evaluated at a current density of 1 C (Figure 6f). S@ZnSe/NHC electrodes displayed an initial high specific capacity of 858.7 mAh g^{-1}. After 200 cycles, 86.6% of the capacity was still retained, 826.9 mAh g^{-1}. In contrast, the S@NHC cathode presented a discharge capacity of 657.8 mAh g^{-1} after 200 cycles (76.1% retention), and the S@Super P cathode showed a capacity of only 516.1 mAh g^{-1} after 200 cycles (67.9% retention). The higher capacity loss in these cathodes was in large part associated to the rapid dissolution of polysulfides into the electrolyte.

Figure 6g presents results from the EIS analysis of the S@ZnSe/NHC cathode before the first discharge and after 200 cycles modeled with equivalent circuits. It can be seen clearly from the fresh cells that the first semicircle in the high frequency is related to the charge transfer resistance (R$_{ct}$) and a linear dependence in the low frequency region that reflected the diffusion of lithium ions into the electrode. Compared with S@NHC (50.2 Ω) and S@Super P (98.5 Ω), S@ZnSe/NHC electrodes showed the lowest R$_{ct}$ (28.6 Ω), which means ZnSe/NHC can facilitate charge transfer, favoring the rapid polysulfide conversion reactions. [29,62] While after 200 cycles, another semicircle in the middle frequency region appears resulted from the deposition of the insulating layer of Li$_2$S on the electrode surface (R$_{int}$). S@ZnSe/NHC electrodes have a considerably lower R$_{int}$ (8.6 Ω) than S@NHC (35.6 Ω) and S@Super P (68.3 Ω) (Figure S24), may attributing to the introduction of ZnSe that catalyze the conversion reactions of polysulfides, thus suppressing the formation of an insulating layer of solid Li$_2$S$_2$/Li$_2$S on the surface of electrodes.

Even at a high current rate of 3 C, S@ZnSe/NHC electrodes displayed stable cycling performance with an average 0.022% capacity decay per cycle after 800 cycles and CEs above 99.5% (Figure 6h). Under the same electrochemical conditions, pure ZnSe/NHC electrodes

showed a negligible capacity (Figure S25). To further demonstrate the potential of S@ZnSe/NHC cathodes for practical applications, a wind car was powered by one S@ZnSe/NHC coin cell, as displayed in Figure 6i.

Coin cells were disassembled after 200 cycles at 1 C. As shown in Figure 6j, after 200 cycles the separator from S@ZnSe/NHC cells exhibited lighter color than that from S@Super P, which indicated that ZnSe/NHC blocked the diffusion of LiPS more effectively. [25] Besides the S@ZnSe/NHC cathode material maintained its original morphology after 200 cycles, demonstrating its excellent structural stability during lithiation/delithiation processes (Figure 6k). In addition, the lithium metal foils from S@ZnSe/NHC showed fewer sulfur signals and less corrosion than those from S@Super P, as displayed by SEM and EDX mapping in Figure 6(l, m). [48]
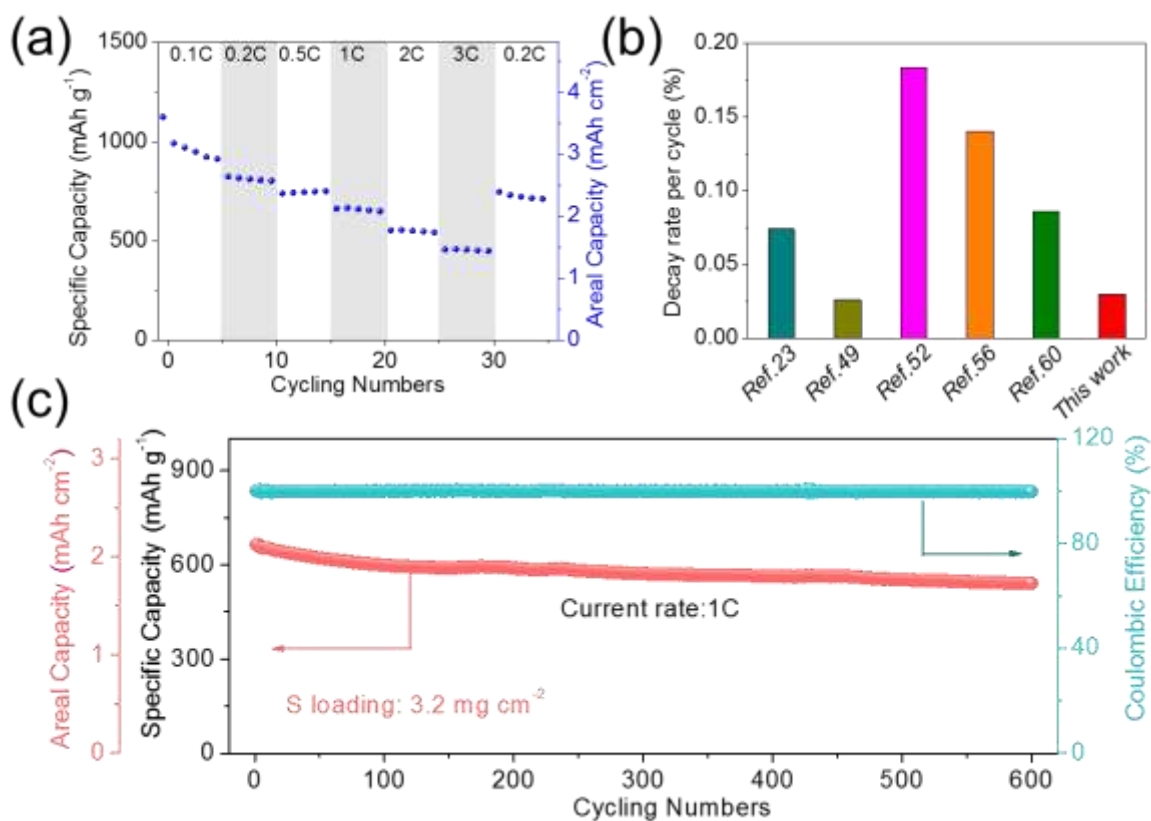
Figure 7. Performance of S@ZnSe/NHC with a high sulfur loading (3.2 mg cm^{-2}): (a) Rate performance. (b) Decay rate per cycle compared with reported works. (c) Cycling performance at 1 C.

To meet the demand for high energy density of practical applications, LSBs should contain high sulfur loadings. Therefore, we studied the performance of S@ZnSe/NHC cathodes at a higher sulfur loading of 3.2 mg cm^{-2}. Figure S26 displays galvanostatic charge/discharge curves of S@ZnSe/NHC cathodes at different current rates. Even at a high current rate of 3 C, the charge plateau and two discharge plateaus were also clearly observed, suggesting a low polarization during charge and discharge processes. At high S loading, S@ZnSe/NHC cathodes delivered a discharge capacity of 1125.72 mAh g^{-1} at 0.1 C and 57.7 mAh g^{-1} at 3 C, which corresponded to areal capacities of 3.60 and 1.46 mAh cm^{-2}, respectively (**Figure 7a**). The excellent rate performances could be attribute to high electrical conductivity and superior catalytic properties of ZnSe/NHC. Long-term cycling tests of S@ZnSe/NHC cathodes with 3.2 mg cm^{-2} of sulfur showed a discharge capacity of 540.5 mAh g^{-1} to be maintained after 600 cycles, with a 0.03% average capacity decay per cycle. Moreover, a high and steady CE above 99.8% was also maintained after long-term cycling, demonstrating an excellent cycling stability (Figure 7c). Compared with other sulfur host materials reported in literatures, the S@ZnSe/NHC cathode showed a high electrochemical performance (Table S1)and lower decay rate per cycle compared with other works even at a high sulfur loading (Figure 7b). [23,50,55,59,63]

3. Conclusions

In summary, we rationally designed new LSBs cathodes based on ZnSe/NHC sulfur hosts with dual effect adsorption and high catalytic activity. Their hollow nanoreactor geometry not only provide an accommodation for sulfur, but also integrates LiPS physical separation and chemical reaction in one cell towards high stable cyclability. ZnSe with sulfiphilic sites and NHC with lithiophilic sites, respectively, were confirmed by experimental results and DFT calculations, showing a strong LiPS adsorbability. Simultaneously, ZnSe nanoparticles could facilitate redox kinetics of LiPS conversion reaction during charge/discharge processes that were revealed by tremendous kinetic investigations, thus improving the sulfur utilization. These merits contribute to outstanding electrochemical performances of the LSBs with ZnSe/NHC as sulfur hosts. As a result, S@ZnSe/NHC cathode delivers excellent performances, including a reversible capacity of 540.5 mAh g^{-1} after 600 cycles at 1 C at a relatively high sulfur loading of 3.2 mg cm^{-2}. This work not only broadens the application of selenides materials in the field of LSBs, but also

designs dual effect adsorptive nanoreactor serving as sulfur hosts, showing superior electrochemical properties for LSBs.

4. Experimental Section

Synthesis of zeolitic imidazolate framework (ZIF-8): 5.95 g (0.02 mol) of $Zn(NO_3)_2 \cdot 6H_2O$ (98%, Alfa Aesar) was dissolved in 150 mL methanol. The obtained solution was poured into 150 mL of a methanol solution containing 6.16 g (0.075 mol) of 2-methylimidazole (99%, Acros Organics) and the mixed solution was stirred for 24 h at room temperature. The obtained white precipitate was collected, washed with methanol several times and dried overnight.

Synthesis of ZnSe/NHC: 100 mg of the as-obtained ZIF-8 powder and 250 mg of selenium powder (99%, Sigma Aldrich) were placed in two separated porcelain boats. The porcelain boats were placed within a tubular furnace having an Ar flow (100 mL·min^{-1}), with the selenium boat upstream and the ZIF-8 powder downstream. The furnace was heated to 650 °C at a heating rate of 5 °C min^{-1} and maintained at this temperature for 2 h. After cooling to room temperature, the ZnSe/NHC powder was collected.

Synthesis of NHC: NHC was obtained by annealing ZIF-8 powder in the same conditions but without selenium. The obtained black powder was immersed in a 2 M HCl solution and stirred for 24 h to remove Zn. The precipitate was collected by filtration, washed with ethanol and dried at 60 °C overnight.

Synthesis of S@ZnSe/NHC, S@NHC and S@Super P: Sulfur was incorporated by means of a simple melting diffusion process. To obtain S@ZnSe/NHC, as-prepared ZnSe/NHC and sublimed sulfur (99.98%, Sigma Aldrich) were well mixed at a 1:3 weigh ratio and heated at 155 °C for 12 h in a glass bottle under an Ar atmosphere. To remove the redundant sulfur outside of ZnSe/NHC, the powder was immersed in a 10 mL CS_2 and ethanol solution (1:4, volume ratio) for 10 min twice. For comparison, S@NHC and S@Super P (Super P from Alfa Aesar, 99%) were obtained by the same process.

Materials Characterization: Chemical compositions were analyzed by X-ray diffraction (XRD) patterns recorded at room temperature using a Bruker AXS D8 Advance X-ray diffractometer with Cu K radiation (λ = 1.5106 Å) operating at 40 kV and 40 mA. Field emission scanning electron microscopy (FESEM) analyses were carried on a ZEISS Auriga microscope with an energy dispersive X-ray spectroscopy (EDS) detector operating at 20 kV. Transmission electron

microscopy (TEM) characterization was carried out on a Zeiss Libra 120 (Carl Zeiss, Jena, Germany) operating at 120 kV. High-resolution TEM (HRTEM) and scanning TEM (STEM) studies were carried out using a field emission gun FEI Tecnai F20 microscope at 200 kV with a point-to-point resolution of 0.19 nm. High angle annular dark-field (HAADF) STEM was combined with electron energy loss spectroscopy in the Tecnai microscope by using a Gatan Quantum filter. X-ray photoelectron spectroscopy (XPS) measurements were conducted at 150 W using a Phoibos 150 MCD-9 detector. Thermogravimetric measurements (TGA) were performed to record the ration of S within prepared composites. UV–vis absorption spectra were tested on a PerkinElmer LAMBDA 950 UV–vis spectrophotometer. Nitrogen adsorption-desorption isotherms were measured to evaluate the specific surface area and the pore size distribution using a Brunauer–Emmett–Teller method (Tristar II 3020 Micromeritics system).

Electrochemical measurements: Working electrodes were prepared by mixing the active materials (S@ZnSe/NHC, S@NHC and S@Super P), Super P and PVDF binders with a weight ratio of 8:1:1 in N-methyl-2-pyrrolidone (NMP, 99.5%, Acros Organics). Then the slurry was coated on an aluminum foil and dried at 60 °C under vacuum overnight. Subsequently, the coated aluminum foil was punched into small disks having a sulfur loading of about 1mg cm^{-2} and were assembled into coin cells in an Ar-filled glovebox. Li foil was used as the counter electrode and Celgard 2400 membranes as separators. The electrolyte was prepared by dissolving 1.0 M lithium bis(trifluoromethanesulfonyl) imide (LiTFSI) (99%, Acros Organics) in a mixture of 1,3-dioxolane (DOL, 99.5%, Alfa Aesar) and dimethoxymethane (DME, 99%, Honeywell) (1:1 v/v) with the addition of 0.2 M LiNO$_3$ (99.98%, Alfa Aesar). The amount of electrolyte was about 20 μL for each coin cell. Before cycling, all coin cells were aged for several hours to ensure a sufficient penetration of the electrolyte into the electrode. Galvanostatic charge/discharge (GCD) measurements were performed with a voltage window of 1.7–2.8 V vs. Li$^+$/Li at different current densities using a Neware BTS4008 battery cycler. Cyclic voltammetry (CV) tests were performed on a battery tester BCS-810 from Bio Logic at different scan rate in the range of 0.1–0.4 mV s^{-1}. Electrochemical impedance spectroscopy (EIS) tests were carried out using a sinusoidal voltage with amplitude of 10 mV in the frequency range 100 kHz to 0.01 Hz.

Synthesis of Li$_2$S$_4$ Solution and Adsorption Test: Sulfur and Li$_2$S (99.9%, Alfa Aesar) with a molar ratio of 3:1 were added to appropriate amounts of DME and DOL (volume ratio of 1:1)

under vigorous magnetic stirring overnight, until a dark brown solution was formed. For the polysulfide absorption ability test, 20 mg active materials (ZnSe/NHC, NHC and Super P) were immersed into 3.0 mL 10×10^{-3} M Li_2S_4 solution, which was shaken and aged overnight.

Symmetric Cell Assembly and Measurements: The ZnSe/NHC (NHC and Super P) composite was mixed with Super P and PVDF binder with a weight ratio of 8:1:1 in NMP. Then the slurry was coated onto the Al foil and dried at 60 °C for 12 h in a vacuum oven. Two pieces of the same electrode (average loading about 0.5 mg cm^{-2}) were used as identical working and counter electrodes. 40 µL of electrolyte containing 0.5 M Li_2S_6 and 1 M LiTFSI dissolved in DOL/DME (v/v = 1/1) was added into each coin cell. CV measurements were performed at scan rate of 10 mV s^{-1} and EIS tests were carried out in the frequency range 100 kHz to 0.01Hz.

Measurement of Nucleation and Dissolution of Li_2S: Nucleation and dissolution of Li_2S were studied in standard 2032 coin cells. Equal amounts of ZnSe/NHC, NHC and Super P composites were dispersed in ethanol and then coated on carbon papers, which worked as the cathode. Li foil was used as the counter electrode. 20 µL of 0.25 M Li_2S_8 with 1.0 M LiTFSI in tetraethylene glycol dimethyl ether solution was used as catholyte, and 20 µL of a 1.0 M LiTFSI solution without Li_2S_8 was used as anolyte. Coin cells were held at 2.06 V to reduce the generation of higher order LiPS than Li_2S_4. After that the cells were potentiostatically discharged at 2.05 V until current decreased to 10^{-5} A. The dissolution of Li_2S was tested by assembling fresh coin cells, which were galvanostatically discharged at 0.10 mA until 1.80 V, and subsequently galvanostatically discharged at 0.01 mA to 1.80 V for full transformation of S species into solid Li_2S. Then cells were potentiostatically charged at 2.40 V for the dissolution of Li_2S into soluble LiPS until the charge current was below 10^{-5} A.

Supporting Information

Supporting Information is available from the Wiley Online Library or from the author.

Received: ((will be filled in by the editorial staff))

Revised: ((will be filled in by the editorial staff))

Published online: ((will be filled in by the editorial staff))

References

[1]. A. Manthiram, Y. Fu, S. H. Chung, C. Zu, Y. S. Su, *Chem. Rev.* **2014**, *114*, 11751.

[2]. H.-J. Peng, J.-Q. Huang, X.-B. Cheng, Q. Zhang, *Adv. Energy Mater.* **2017**, *7*, 1700260.

[3]. Z. Li, H. B. Wu, X. W. Lou, *Energy Environ. Sci.* **2016**, *9*, 3061.

[4] H. J. Peng, J. Q. Huang, X. Y. Liu, X. B. Cheng, W. T. Xu, C. Z. Zhao, F. Wei, Q. Zhang, *J. Am. Chem. Soc.* **2017**, *139*, 8458.

[5] G. M. Zhou, L.-C. Yin, D.-W. Wang, L. Li, S. F. Pei, L. R Gentle, F. Li, H.-M. Cheng, *ACS Nano* **2013**, *7*, 5367.

[6] X. Ji, K. T. Lee, L. F. Nazar, *Nat. Mater.* **2009**, *8*, 500.

[7] C. Ye, L. Zhang, C. X. Guo, D. D. Li, A. Vasileff, H. H.Wang, S.-Z. Qiao, *Adv. Funct. Mater.* **2017**, *27*, 1702524.

[8] A. Manthiram, S. H. Chung, C. Zu, *Adv. Mater.* **2015**, *27*, 1980.

[9] J. Schuster, G. He, B. Mandlmeier, T. Yim, K. T. Lee, T. Bein, L. F. Nazar, *Angew. Chem., Int. Ed.* **2012**, *51*, 3591.

[10] M. Yu, R. Li, M. Wu, G. Shi, *Energy Storage Mater.* **2015**, *1*, 51.

[11] Z. Du, X. Chen, W. Hu, C. Chuang, S. Xie, A. Hu, W. Yan, X. Kong, X. Wu, H. Ji, L. J. Wan, *J. Am. Chem. Soc.* **2019**, *141*, 3977.

[12] F. Xu, Z. Tang, S. Huang, L. Chen, Y. Liang, W. Mai, H. Zhong, R. Fu, D. Wu, *Nat. Commun.* **2015**, *6*, 7221.

[13] R. Fang, G. Li, S. Zhao, L. Yin, K. Du, P. Hou, S. Wang, H.-M. Cheng, C. Liu, F. Li, *Nano Energy* **2017**, *42*, 205.

[14] K. Mi, Y. Jiang, J. Feng, Y. Qian, S. Xiong, *Adv. Funct. Mater.* **2016**, *26*, 1571.

[15] S. Lu, Y. Cheng, X. Wu, J. Liu, *Nano Lett.* **2013**, *13*, 2485.

[16] L. Xia, S. Wang, G. Liu, L. Ding, D. Li, H. Wang, S. Qiao, *Small* **2016**, *12*, 853.

[17] H. J. Peng, G. Zhang, X. Chen, Z. W. Zhang, W. T. Xu, J. Q. Huang, Q. Zhang, *Angew. Chem. Int. Ed.* **2016**, *55*, 12990.

[18] X. Wang, G. Li, J. Li, Y. Zhang, A. Wook, A. Yu, Z. Chen, *Energy Environ. Sci.* **2016**, *9*, 2533.

[19] Z. Liang, G. Zheng, W. Li, Z. W. Seh, H. Yao, K. Yan, D. Kong, Y. Cui, *ACS Nano* **2014**, 8, 5249.

[20] L. Kong, B.-Q. Li, H.-J. Peng, R. Zhang, J. Xie, J.-Q. Huang, Q. Zhang, *Adv. Energy Mater.* **2018**, *8*, 1800849.

[21] C. Dai, L. Hu, M.-Q. Wang, Y. Chen, J. Han, J. Jiang, Y. Zhang, B. Shen, Y. Niu, S.-J. Bao, M. Xu, *Energy Storage Mater.* **2017**, *8*, 202.

[22] D. R. Deng, F. Xue, Y. J. Jia, J. C. Ye, C. D. Bai, M. S. Zheng, Q. F. Dong, *ACS Nano* **2017**, *11*, 6031.

[23] T. Chen, L. Ma, B. Cheng, R. Chen, Y. Hu, G. Zhu, Y. Wang, J. Liang, Z. Tie, J. Liu, Z. Jin, *Nano Energy* **2017**, *38*, 239.

[24] Z. Xiao, Z. Yang, L. Zhang, H. Pan, R. Wang, *ACS Nano* **2017**, *11*, 8488.

[25] C. Dai, J.-M. Lim, M. Wang, L. Hu, Y. Chen, Z. Chen, H. Chen, S.-J. Bao, B. Shen, Y. Li, G. Henkelman, M. Xu, *Adv. Funct. Mater.* **2018**, *28*, 1704443.

[26] H. Lin, L. Yang, X. Jiang, G. Li, T. Zhang, Q. Yao, G. W. Zheng, J. Y. Lee, *Energy Environ. Sci* **2017**, *10*, 1476.

[27] D. Liu, C. Zhang, G. Zhou, W. Lv, G. Ling, L. Zhi, Q. H. Yang, *Adv. Sci.* **2018**, *5*, 1700270.

[28] C. Zhang, J. J. Biendicho, T. Zhang, R. Du, J. Li, X. Yang, J. Arbiol, Y. Zhou, J. R. Morante, A. Cabot, *Adv. Funct. Mater.* **2019**, *29*, 1903842.

[29] Y. Tian, G. Li, Y. Zhang, D. Luo, X. Wang, Y. Zhao, H. Liu, P. Ji, X. Du, J. Li, Z. Chen, *Adv. Mater.* **2020**, *32*, e1904876.

[30] H. Yuan, H.-J. Peng, B.-Q. Li, J. Xie, L. Kong, M. Zhao, X. Chen, J.-Q. Huang, Q. Zhang, *Adv. Energy Mater.* **2019**, *9*, 1802768

[31] Y. He, L. Wang, C. Dong, C. Li, X. Ding, Y. Qian, L. Xu, *Energy Storage Mater.* **2019**, *23*, 35.

[32] Y. Zhang, W. Qiu, Y. Zhao, Y. Wang, Z. Bakenov, X. Wang, *Chem. Eng. J* **2019**, *375*, 122055.

[33] J. Xu, W. Zhang, H. Fan, F. Cheng, D. Su, G. Wang, *Nano Energy* **2018**, *51*, 73-82.

[34] A. Cabot, M. Ibáñez, P. Guardia, A. P. Alivisatos, *J. Am. Chem. Soc.* **2009**, *131*, 11326.

[35] M. Ibáñez, J. Fan, W. Li, D. Cadavid, R. Nafria, A. Carrete, A. Cabot, *Chem. Mater.* **2011**, *23*, 3095.

[36] S. Lu, T. Zhu, H. Wu, Y. Wang, J. Li, A. Abdelkader, K. Xi, W. Wang, Y. Li, S. Ding, G. Gao, R. V. Kumar, *Nano Energy* **2019**, *59*, 762.

[37] Q. Peng, Y. Dong, Y. Li, *Angew. Chem. Int. Ed.* **2003**, *42*, 3027.

[38] C. Dong, L. Guo, Y. He, C. Chen, Y. Qian, Y. Chen, L. Xu, *Energy Storage Mater.* **2018**, *15*, 234.

[39] D. Su, K. Kretschmer, G. Wang, *Adv. Energy Mater.* **2016**, *6*, 1501785.

[40] Y. He, M. Luo, C. Dong, X. Ding, C. Yin, A. Nie, Y. Chen, Y. Qian, L. Xu, *J. Mater. Chem. A* **2019**, *7*, 3933.

[41] M. Wan, R. Zeng, K. Chen, G. Liu, W. Chen, L. Wang, N. Zhang, L. Xue, W. Zhang, Y. Huang, *Energy Storage Mater.* **2018**, *10*, 114.

[42] C. Dong, J. Liang, Y. He, C. Li, X. Chen, L. Guo, F. Tian, Y. Qian, L. Xu, *ACS Nano* **2018**, *12*, 8277.

[43] M. Mao, C. Cui, M. Wu, M. Zhang, T. Gao, X. Fan, J. Chen, T. Wang, J. Ma, C. Wang, *Nano Energy* **2018**, *45*, 346.

[44] Z. R. Ismagilov, A. E. Shalagina, O. Y. Podyacheva, A. V. Ischenko, L. S. Kibis, A. I. Boronin, Y. A. Chesalov, D. I. Kochubey, A. I. Romanenko, O. B. Anikeeva, T. I. Buryakov, E. N. Tkachev, *Carbon* 2009, *47*, 1922.

[45] J. D. Wiggins-Camacho, K. J. Stevenson, *J. Phys. Chem. C* **2009**, *113*, 19082.

[46] Z. Li, J. Zhang, H. B. Wu, X. W. D. Lou, *Adv. Energy Mater.* **2017**, *7*, 1700281.

[47] J. Song, Z. Yu, M. L. Gordin, D. Wang, *Nano Lett.* **2016**, *16*, 864.

[48] X. Li, K. Ding, B. Gao, Q. Li, Y. Li, J. Fu, X. Zhang, P. K. Chu, K. Huo, *Nano Energy* **2017**,

40, 655.

[49] L. Hu, C. Dai, H. Liu, Y. Li, B. Shen, Y. Chen, S.-J. Bao, M. Xu, *Adv. Energy Mater.* **2018**, *8*, 1800709.

[50] Y. Qiu, W. Li, W. Zhao, G. Li, Y. Hou, M. Liu, L. Zhou, F. Ye, F. Li, Z. Wei, S. Yang, W. Duan, Y. Ye, Y. Guo, Y. Zhang, *Adv. Mater.* **2014,** *14,* 4281.

[51] M. Yan, H. Chen, Y. Yu, H. Zhao, C.-F. Li, Z.-Y. Hu, P. Wu, L. Chen, H. Wang, D. Peng, H. Gao, T. Hasan, Y. Li, B.-L. Su, *Adv. Energy Mater.* **2018**, *8*, 1801066.

[52] L. Zhang, X. Chen, F. Wan, Z. Niu, Y. Wang, Q. Zhang, J. Chen, *ACS Nano* **2018**, *12*, 9578.

[53] B. Yuan, D. Hua, X. Gu, Y. Shen, L.-C. Xu, X. Li, B. Zheng, J. Wu, W. Zhang, S. Li, F. Huo, *J. Energy. Chem.* **2020**, *48*, 128.

[54] X. Li, B. Gao, X. Huang, Z. Guo, Q. Li, X. Zhang, P. K. Chu, K. Huo, *ACS Appl. Mater. Interfaces* **2019**, *11*, 2961.

[55] X. Zhu, W. Zhao, Y. Song, Q. Li, F. Ding, J. Sun, L. Zhang, Z. Liu, *Adv. Energy Mater.* **2018**, *8*, 1800201.

[56] Z. Yuan, H. J. Peng, T. Z. Hou, J. Q. Huang, C. M. Chen, D. W. Wang, X. B. Cheng, F. Wei, Q. Zhang, *Nano Lett.* **2016**, *16*, 519-27.

[57] G. Zhou, H. Tian, Y. Jin, X. Tao, B. Liu, R. Zhang, Z. W. Seh, D. Zhuo, Y. Liu, J. Sun, J. Zhao, C. Zu, D. S. Wu, Q. Zhang, Y. Cui, *Proc. Natl. Acad. Sci. USA* **2017**, *114*, 840.

[58] A. Berger, A. T. S. Freiberg, A. Siebel, R. Thomas, M. U. M. Patel, M. Tromp, H. A. Gasteiger, Y. Gorlin, *J. Electrochem. Soc.* **2018**, *165*, A1288.

[59] S. Huang, Y. V. Lim, X. Zhang, Y. Wang, Y. Zheng, D. Kong, M. Ding, S. A. Yang, H. Y. Yang, *Nano Energy* **2018**, *51*, 340.

[60] C.-Y. Fan, Y.-P. Zheng, X.-H. Zhang, Y.-H. Shi, S.-Y. Liu, H.-C. Wang, X.-L. Wu, H.-Z. Sun, J.-P. Zhang, *Adv. Energy Mater.* **2018**, *8*, 1703638.

[61] D. Su, M. Cortie, H. Fan, G. Wang, *Adv. Mater.* **2017**, *29*, 1700587.

[62] Z. Guo, H. Nie, Z. Yang, W. Hua, C. Ruan, D. Chan, M. Ge, X. Chen, S. Huang, *Adv. Sci.* **2018**, *5*, 1800026.

[63] M. Yu, J. Ma, H. Song, A. Wang, F. Tian, Y. Wang, H. Qiu, R. Wang, *Energy Environ. Sci.* **2016**, *9*, 1495.